b-tagging at LHC

T. Mouthuy, a N. Rozanov, L. Vacavant

▶ To cite this version:

b-tagging at LHC

Thierry Mouthuy [*], Alexander Rozanov [†]and Laurent Vacavant [‡]

CNRS-IN2P3/CPPM, 163 av. de Luminy, Case 907,

13288 Marseille Cedex 09, France

Abstract

The review of the recent progress in the area of b-tagging studies at LHC is presented. Vertex b-tagging will be the major tool for the search for low mass Higgs both in the Standard Model scheme and in its Supersymmetric extensions at LHC experiments. The simulation results indicate that the rejection of gluon and light quark jets of $R_{q/g-jet} = 50$ with b-tagging efficiency $\epsilon_{b-jet} = 50\%$ can be achieved at LHC experiments.

[*]mouthuy@cppm.in2p3.fr

[†]corresponding author, rozanov@cppm.in2p3.fr

[‡]vacavant@cppm.in2p3.fr

1 Introduction

The importance of b-tagging for LHC physics increased in the last years. Partly it was due to the success by the CDF Collaboration at the Fermilab Tevatron collider in the effective use of the b-tagging in the discovery of the top quark. In addition, more arguments favour the search for relatively light standard or supersymmetric Higgs bosons. Many of these Higgs bosons decay into final states with b-quarks. Both ATLAS [1] and CMS [2] Collaborations plan to build the vertex detectors near the interaction point in order to achieve the best b-tagging performance.

2 B-physics and b-tagging

In the process of the design of the LHC experiments two important directions should be distinguished in the area of physics with b-flavour identifications. First of these directions is a wide program of B-physics studies. It includes [3, 4] in particular the measurement of CP violation in $B_d^0 \to J/\Psi K_s^0, B_d^0 \to \pi^+\pi^-$ and $B_s^0 \to J/\Psi\phi$ decays. The time dependent asymmetry in the $B_d^0 \to J/\Psi K_s^0$ decay is directly proportional to the $\sin 2\beta$ parameter. β is one of the angles of the unitarity triangle presentation of the Cabibbo-Kobayashi-Maskawa (CKM) quark mixing matrix, which is approximately proportional to the CP violation phase η. At present the constraints on β from K- and B-meson decays [5] within Standard Model are $5° \leq \beta \leq 45°$. The angle α in the unitarity triangle is measured in the time dependent asymmetry of the $B_d^0 \to \pi^+\pi^-$ decay, which is experimentally more difficult due to the absence of J/Ψ tag. The CP violation parameter η will be also measured in the time-dependent asymmetry of the $B_s^0 \to J/\Psi\phi$ decay.

Another major goal is the observation of $B_s^0 - \bar{B}_s^0$ mixing with $B_s^0 \to D_s^+K^-$ and $\bar{B}_s^0 \to D_s^-K^+$ predicted in the Standard Model. Rare B-decays, for example $B_s^0 \to \mu^+\mu^-$ will be used for tests of physics beyond the Standard Model. Progress in the measurement of B-hadron cross-sections, polarisation and spectroscopy is expected due to the high $b\bar{b}$ rate.

The typical properties of the B-physics studies at LHC are:

- Exclusive final states of the processes have to be studied.

- Rather low average p_T around 12 GeV.

- High cross-sections of 0.5 mb with $5 \times 10^{12} b\overline{b}$ pairs per year at $L = 10^{33} \mathrm{cm}^{-2} \mathrm{s}^{-1}$.

- Reconstruction of 3-dimensional vertex is important.

- Lifetime accuracy is needed for the measurement of the time-dependent CP-asymmetry.

B-physics will be the main issue for the LHC-B [6] experiment, but both general purpose ATLAS [1] and CMS [2] experiments plan to perform these measurements at LHC. The specialized HERA-B [7], Ba-BAR [8] and BELLE [9] experiments will perform these measurements at lower energy accelerators.

The second direction is the b-tagging of the high-p_T jets, originating from b-quark fragmentation and decay. These b-quark jets are produced in the decay of heavy particles like t-quark or Higgs boson. Typical decay is H $\rightarrow$ b$\overline{\mathrm{b}}$ with Higgs mass in the range 80-130 GeV. The main goal is to discriminate these rare events with b-quarks in the final state from the much larger background of light quarks and gluons. This requires good b-tagging efficiency together with high rejection of non-b jets.

The main features of b-tagging physics at LHC can be summarised as:

- High p_T of b-jets around 50 GeV and above.

- Low cross-sections of b-tagged events.

- High background from light quark and gluon jets.

- Reconstruction of 3-dimensional vertex is optional.

- The number of b-jets in final states ranges from two to four.

- Lifetime accuracy is not critical.

- c-jet background is moderate, because c-quark production cross-section is similar to b-quark production.

- Soft lepton tag (p_T around 1-2 GeV) could be the complementary way to improve the overall b-tagging performance.

These features are rather different from B-physics and they require special attention in the detector design and performance studies. In the following we will concentrate on the b-tagging at LHC.

3 Search for Higgs at LHC

The most important issue for the LHC is the search for the Higgs boson, required to understand the mechanism of the spontaneous symmetry-breaking and the origin of masses. Therefore the Higgs search is used as a benchmark for the detector optimisation. Many Higgs boson decays involve b-quark final states:

- $H \to b\overline{b}$ from WH or $t\overline{t}$ H production in the Standard Model (SM).

- $h \to b\overline{b}$ from Wh or $t\overline{t}$ h. production in the Minimal Supersymmetric Standard Model (MSSM).

- $H \to hh \to b\overline{b}$ $\gamma\gamma$ in MSSM.

- $H \to hh \to b\overline{b}$ $b\overline{b}$ in MSSM.

- $A \to Zh \to l\overline{l} b\overline{b}$ and $A \to Zh \to b\overline{b}$ $b\overline{b}$ in MSSM.

- $A \to t\overline{t}$ and $H \to t\overline{t}$ in MSSM.

The decay $H \to b\overline{b}$ is the dominant mode in case the Higgs mass is below 130 GeV. Recent fits to all electroweak precision data, including the top quark mass from Fermilab, favour low value of the Higgs mass. For example, the fit with LEPTOP package [10] to the published electroweak results [11] together with Fermilab top mass of $m_t = 180 \pm 12$ GeV and strong coupling constant $\hat{\alpha}_s = 0.124$ is shown on Fig. 1. The most probable value from the fit is $m_H = 74$ GeV, but the error is still very big, so at the level of two standard deviations the Higgs mass could be as big as 1000 GeV. However this prediction strongly motivate us to explore all the possibilities to search Higgs boson with the mass below 130 GeV. This motivation is even more supported by the prediction [12], that for MSSM

4

case the lightest Higgs boson should have its mass below 145 GeV. The actual direct limit on Higgs mass from ALEPH LEP experiment is 63.9 GeV [13] and the limit reachable at LEP-II would be around 85 GeV. This defines the interesting region for Higgs mass range $80 < m_{\mathrm{H}} < 130$ GeV for the search of the decay $\mathrm{H} \rightarrow \mathrm{b\overline{b}}$ at LHC. Other channels like $\mathrm{H} \rightarrow \gamma\gamma$, $\mathrm{H} \rightarrow \mathrm{Z}\gamma$, $\mathrm{H} \rightarrow \mathrm{ZZ}^* \rightarrow \mathrm{l\overline{l}l\overline{l}}$ are possible [1, 2] in some regions of this mass range, but due to the lack of statistics and high backgrounds they need confirmation from different channels.

3.1 Search for Standard Model Higgs in WH channel

Association production of Higgs with W, Z or $\mathrm{t\overline{t}}$ is needed to provide isolated lepton to trigger experiment and reduce large $\mathrm{b\overline{b}}$ background. Production cross-section and rates of $\mathrm{u\overline{d}} \rightarrow \mathrm{W}^* \rightarrow \mathrm{WH} \rightarrow l\nu\,\mathrm{b\overline{b}}$ and $\mathrm{gg} \rightarrow \mathrm{t\overline{t}\,H} \rightarrow \mathrm{WW\,b\overline{b}\,b\overline{b}}$ were calculated by D.Froidevaux and E.Richter-Was [14] for the following selection criteria:

- Lepton with transverse momentum $p_T{}^{\mu} > 6$ GeV or $p_T{}^e > 30$ GeV, pseudo-rapidity $\eta^l < 2.5$ is isolated from any selected jet by $\Delta R = \sqrt{\Delta\eta^2 + \Delta\phi^2} > 0.7$.

- Two b-jets have $p_T{}^{b-jet} > 15$ GeV and $\eta^{b-jet} < 2.5$ with isolation between b-jets and lepton $\Delta R_{bb,bl} > 0.7$.

- Lepton veto is required on any other isolated lepton with $p_T{}^l > 6$ GeV, $\eta^l < 2.5$.

- Jet veto: no more jet exists with $p_T{}^{jet} > 15$ GeV, $\eta^{jet} < 5.0$

The signal of $\mathrm{H} \rightarrow \mathrm{b\overline{b}}$ appears as a peak in the invariant mass distribution of two b-jets on top of very large background. Due to the effects of the final state radiation and hadronization the peak is shifted by approximately 10 GeV to lower value of the mass.

Backgrounds to $\mathrm{WH} \rightarrow l\nu\,\mathrm{b\overline{b}}$ can be classified as irreducible, when the final state is the same as in Higgs production, or reducible, when there are additional or misidentified particles:

- Irreducible resonant background $\mathrm{WZ} \rightarrow l\nu\,\mathrm{b\overline{b}}$

5

- Irreducible non-resonant background $q\overline{q} \to Wg \to W\ b\overline{b} \to l\nu\ b\overline{b}$.

- Reducible backgrounds with two b-quarks $gg \to t\overline{t} \to l\nu\ b\overline{b} + W$ and $qg \to t\ \overline{b}\ q \to l\nu\ b\overline{b} + q$.

- Reducible backgrounds with b-jet misidentification by light quark or gluon jets $Wjj \to l\nu b_{false}\overline{b}_{false}$. Here the quality of the b-tagging is crucial.

Production cross-sections and rates of Higgs with $m_H = 100$ GeV and backgrounds including branching ratios according to [14] for one year of low luminosity LHC run with $L = 10^4 \text{pb}^{-1}$ are shown in the Table 1. Relatively small rate of Higgs production requires the decent efficiency of b-jet tagging ϵ_b, while very high background requires the rejection factor of light and gluon jets R to be as high as possible. In practice the rejection R bigger than 100 is not needed, because the irreducible background with $b\overline{b}$ final states starts to dominate in this case. Taking $R = 50$ at efficiency $\epsilon_b = 50\%$ the significance of the Higgs signal with $m_H = 80$ GeV is $S/\sqrt{B} = 2.1$ standard deviation. The conclusion is that, the background dictates the requirement for the b-tagging rejection of at least $R = 50$ at efficiency $\epsilon_b = 50\%$. These numbers will be used for numerical estimates and confronted with the results of the full GEANT simulation.

3.2 Search for Standard Model Higgs in $t\overline{t}$ H channel

The final state for that channel is more complicated as it contains $WW\ b\overline{b}\ b\overline{b}$. Higgs signal appears as the peak in $b\overline{b}$ invariant mass spectra on top of the combinatorial background of 4 b-jets from the same signal events plus irreducible backgrounds from $t\overline{t}$ Z channel, $t\overline{t}\ b\overline{b}$ and reducible backgrounds with misidentified b-jets from $t\overline{t}$ j, Wjjj, W $b\overline{b}$ j etc. The selection criteria are the same as for WH events plus the requirement to find at least 3 isolated b-jets with $p_T^{b-jet} > 16$ GeV and $\eta^{b-jet} < 2.5$.

Again taking $R = 50$ at efficiency $\epsilon_b = 50\%$ the significance of the Higgs signal with $m_H = 80$ GeV in $t\overline{t}$ H channel is $S/\sqrt{B} = 2.3$ standard deviation. This means that $t\overline{t}$ H channel should be treated

as complementary to WH channel for low mass Higgs search at LHC. The importance of that channel even increases at high luminosity, where WH, H $\rightarrow$ b$\overline{\text{b}}$ channel is considered impossible, because it needs a very tight jet veto cut to reject t$\overline{\text{t}}$ background.

3.3 Combination of Standard Model Higgs channels

It is likely, that during the first three years of low luminosity operation of LHC the integrated luminosity would reach $L = 3 \times 10^4 \text{pb}^{-1}$. In ATLAS Technical Proposal [1] the combination of all Higgs channels in the difficult range of $80 < m_\text{H} < 120$ GeV was made. One can see from the Table 2 that during the first years of ATLAS LHC running it would be difficult to establish a signal of the Higgs of low mass in one particular channel, but the combination of all channels could provide the evidence for it. It is also true for CMS [2], where the significance of H $\rightarrow \gamma\gamma$ channel in low luminosity runs , corrected to the same assumptions of the cross-sections and cuts in [15] is higher by a factor of 1.3, due to the better resolution of the proposed PbWO$_4$ crystal calorimeter. This difference is reduced below 10% level for high luminosity runs.

For the high luminosity run with $L = 10^5$ pb^{-1}, summarised in the Table 3, the same b-tagging efficiency and non-b jet rejection are assumed. This puts the performance requirement on the b-tagging layer in the high luminosity run. Even at high luminosity run, where H $\rightarrow \gamma\gamma$ channel has higher significance, H $\rightarrow$ b$\overline{\text{b}}$ dominates in sensitivity at low Higgs masses.

3.4 Supersymmetric Higgs

Higgs sector is more complicated in case of the supersymmetric extension of the Standard model. In the Minimal Supersymmetric Standard Model there are three neutral states, h - light scalar, H - heavy scalar, A - pseudo-scalar and two charged H$^+$ and H$^-$ states. At the tree level, all Higgs masses can be expressed in terms of two parameters m_A and $\tan\beta$. The dominant decay mode of the lightest Higgs is h $\rightarrow$ b$\overline{\text{b}}$, which determines the importance of b-tagging in MSSM studies. The extended calculations of the rates, background and significances expected in the search for MSSM Higgs at LHC

with ATLAS detector is given in [16]. The following supersymmetric Higgs channels with b-tags are observable at LHC:

- $Wh \to b\bar{b}$ is observable at $\tan \beta < 3$. and $m_A = 100 \div 150$ GeV at 5 standard deviation level.

- $H \to hh \to b\bar{b} \gamma\gamma$ is observable at $\tan \beta < 2$. and $m_A = 175 \div 350$ GeV at 5 standard deviation level.

- $A \to Zh$ is observable at $\tan \beta < 3$. and $m_A = 200 \div 350$ GeV at 5 standard deviation level. This channel is dominant for $m_Z + m_h < m_A < 2m_t$.

- $A/ H \to t\bar{t}$ is observable at $\tan \beta < 1.5$ and $m_A = 350 \div 380$ GeV at 5 standard deviation level. This channel is dominant for $m_H > 2m_t$.

It should be noted, that without b-tagged Higgs channels an important region in the parameter space $3. < \tan \beta < 9.$ and $m_A = 110 \div 300$ GeV is not fully covered by other channels. This fact also stimulates ATLAS and CMS collaborations to install high performance vertex layer for b-tagging.

4   Vertex detectors for b-tagging

The b-tagging performance of the LHC detectors is mainly defined by the innermost tracking detectors. Both ATLAS and CMS detectors have chosen to place few layers of silicon pixel detectors close to the interaction region.

4.1   ATLAS pixel detector

Pixel detector of the ATLAS inner tracker consists of the barrel tracker and two symmetric end-cap trackers. The barrel tracker is made of three cylindrical pixel layers at 4.0, 11.0 and 14.2 cm radius. The dimension of the active zone in z is ± 38.4 cm. The z-cut of the barrel pixel detector is shown on fig. 2. The layer at 4 cm is called b-layer and it consists of 16 ladders. This layer should be operational during the initial low luminosity LHC runs. An alternative strip b-layer at the radius of 6 cm is also discussed and the choice between

them should be made before the end of 1996. The layer at 11 cm will be the first pixel layer during the high luminosity LHC runs, unless new radiation hard detectors, like SVD diamond, would be available for 4 cm b-layer. The pixel size has been chosen to be 50μm in the transverse coordinate and 300μm in the longitudinal Z coordinate. The end-cap tracker has two identical mirror reflected trackers. Each of the end-cap trackers consists of four wheels at z=47.3, 63.5, 77.6 cm and 107.2 cm. The radial active area of the 3 disks is from 11.0 cm up to 20.8 cm, for the fourth disk it is only from 15.9 cm up to 20.8 cm. The disk will use the pixels of the same size as barrel, with 50μm pitch in ϕ coordinate and 300μm pitch in R coordinate. The radial cut of the pixel detector together with other inner detectors is shown on fig. 3. The details of the current geometry of ATLAS pixel can be found in Ref. [17].

4.2 CMS pixel detector

In the CMS pixel detector the two barrel layers will be at the radii of 7.7 cm and 11.7 cm. The active coverage in Z is ±32.5 cm. Square pixel shape $125 \times 125\mu$m with staggering the adjacent z rows was chosen. The high magnetic field of 4 T in CMS is responsible for the Lorentz angle of $34°$, which is by a factor of two bigger than in ATLAS and results in large charge spreading in the r-ϕ direction without special tilt angle. Three disks in both directions positioned at z=39, 54 and 69 cm cover the radial region from 7.5 to 15 cm. The pixel pith and orientation were chosen the same as in the ATLAS disks. Staggering of the adjacent pixels in r direction is envisaged. More details on the design and performance of CMS pixel system can be found in the contribution of R.Horisberger [18].

4.3 Impact parameter resolution

b-tagging performance at LHC is based on the impact parameter resolution of the vertex layers of the inner detector. In case of AT-LAS detector the impact parameter resolutions for different variants of the vertex layouts is given in the Table 4. These parametrisations should be valid in the barrel part of the tracker at $|\eta| < 1.5$. The transverse impact-parameter resolutions, σ_{ip}, are similar for the

various layouts.

The parametrisations given above were obtained with the simplified model of the inner detector. Full GEANT simulation and reconstruction are now available, taking into account many tiny geometrical and physical effects, including the details of the material budget distribution shown on fig 4. The simulations were done for pixel b-layer with binary readout of 150μm thick silicon detectors with the effective threshold of 2000 electrons. The effect of the charge sharing with Lorentz angle were included. The resulting resolutions on transversal and longitudinal impact parameters are shown on fig. 5 for muons with $p_T = 100$ GeV and for muons with $p_T = 1$ GeV. The analytical parametrisations from ATLAS Technical Proposal, shown as the continuous curves, are close to full Monte-Carlo results. The effect of the charge sharing and inclusion of pixel disks at high η are responsible for deviations from these simple parametrisations.

At hight p_T and in the barrel region CMS tracker [2] has similar impact parameter resolution of $\sigma_{R\phi} = 20\mu$m and $\sigma_Z = 90\mu$m. At higher pseudo-rapidity $|\eta| = 2.25$ it increases up to $\sigma_{R\phi} = 29\mu$m and $\sigma_Z = 320\mu$m probably due to the shorter pseudo-rapidity coverage of the first barrel pixel layer. CMS tracker also shows stronger loss of the resolution due to the multiple scattering for tracks with $p_T < 10$ GeV/c, mainly because its first pixel layer is located at a larger radius of 7.7 cm.

4.4 Preliminary test beam results of ATLAS pixels

In May 1996 a prototype of the ATLAS pixel detectors with CPPM readout scheme [19] was tested in the pion beam at CERN. This chip was produced in the DMILL radiation hard technology with binary readout scheme and shift-register storage. The readout frequency of 40 MHz with hit selection in one bunch crossing (BCO) of 25 ns was used. This test chip has 63 rows $\times$ 12 columns pixel matrix. Pixel size was 50 μm by 432 μm. The residuals between the prediction from the silicon strip telescope and the position of the pixel cluster show approximately flat distribution of 430 μm for column side (Fig. 7) and of 50 μm for row side (Fig. 8). The Gaussian fit of residuals on the row side give the resolution of 16μm. On

the bottom of the figures the histograms of the residuals with the selection two pixel clusters show a resolution of 10-12 μm for both column and row sides. More tests of LHC pixels chips are planned in 1996-97 before the final design will be chosen.

5   b-tagging algorithms

All vertex b-tagging algorithms are based on pattern recognition programs, which allow to reconstruct the track impact parameters in the context of the complicated events with high charged track multiplicity. In the context of ATLAS and CMS collaboration several pattern recognition programs [20], [21], [22] are used to probe the relative merits of different approaches. We used the simple combinatorial pattern recognition proposed by T.Mouthuy [23], where each pixel in the first pixel layer is used as the starting point for the combinatorial pattern recognition. The method use the hyperplane concept, where several detector elements in the barrel and end-cap parts are combined into hermetic and efficient hyper-plane. This approach exploits the fine pixel granularity and low occupancy. The program PTRA is integrated into the interactive GEANT [24] environment, uses AGE [25] language and data structures. PTRA extensively uses ATRECON [26] ATLAS reconstruction package.

Track finding efficiencies of the PTRA pattern recognition program have been estimated on the sample of H $\rightarrow$ b$\overline{\text{b}}$ events in the barrel region. The results are presented in the Table 5.

Similar track finding efficiencies of $90 - 95\%$ were obtained with XKAL pattern recognition [27], which is based on the continuous Transition Radiation Tracker (TRT) and uses Kalman filter method in the precision tracker.

The most popular vertex b-tagging algorithms used in LHC experiments are:

- ALEPH-like algorithm. One-sided Gaussian probability for each track: $\omega = \frac{2}{\sqrt{2\pi}} \int_d^{\infty} \exp -\frac{x^2}{2\sigma^2} dx$
  where σ_d is the measurement accuracy of d.
  For all tracks the combined probability $P = \prod_i^n \omega_i$. Normalised probability $\Omega = P \sum_{j=0}^{n-1} \frac{(-\ln P)^j}{j!}$

The cut on Ω provides discrimination of b-jets.

- Track counting algorithm. Count tracks on signed impact parameter $3\sigma_d < d < 1$ mm. Upper limit on the impact parameter rejects many K_s^0 and Λ.
  A cut on the number of particles provides discrimination of b-jets.

- Probability ratio algorithm. Global likelihood ratio based on the distribution of impact parameter d expected for b-jets and gluon-jets: $P_b(d)$ and $P_g(d)$.
  $R = \sum_1^n \ln \frac{P_b(d)}{P_g(d)}$ provides discrimination of b-jets.

We noted that simple track counting usually gives better results, while ALEPH-like algorithm works better in the special case of the absence of K_s^0 and Λ in the data. This indicates that special program for K_s^0 and Λ recognition might improve the result. It was shown in the Ref. [27] that the track counting and probability ratio algorithms give similar results.

6 b-tagging performance

In order to check, that the required b-tagging efficiency and rejection meet the specifications set by physics, it is convenient to use as a benchmark $H \rightarrow b\overline{b}$ and $H \rightarrow gg$ decay channels. In this way we can test and optimise the detector on the most interesting physical channel. Gluon decays of Higgs serve to model the biggest two jet background. We used Higgs with $m_H = 100$ GeV in the full GEANT simulation and ATRECON reconstruction with PTRA pattern recognition for $H \rightarrow b\overline{b}$ and $H \rightarrow gg$ events in the ATLAS detector for low-luminosity LHC run.

In the absence of multiple scattering and secondary interactions, the signed transverse impact parameter distribution of the tracks coming from gluon jets are clearly distinguished (Fig. 9(a)) from the same distributions coming from b-jets (Fig. 9(b)). In the realistic case with multiple scattering and secondary interactions (Fig. 10) the corresponding distributions are smeared, but still distinguishable.

On the Fig. 11 the gluon-jet rejection is plotted versus b-jet efficiency using track counting method. Partial GEANT simulation without secondary interaction, but including energy loss and multiple scattering are show a open circles. For 50% b-jet tagging efficiency the gluon jet rejection factor is $R_{g-jet} = 60$. Including all secondary interactions with full GEANT simulation the b-jet rejection factor is reduced to $R_{g-jet} = 45$. This result is very close to the rejection factor $R_{g-jet} \sim 50$, obtained by I.Gavrilenko [27] for full GEANT simulation and XKAL reconstruction with probability ratio method and slightly different detector layout.

Similar results were obtained with simplified fast simulations by S.Haywood [28] and T.Mouthuy [23].

CMS Collaboration [2] obtains in the partial simulation the rejection factor for light quarks and gluon jets $R_{q/g-jets} = 53$ keeping the efficiency of b-jet tagging from $t\bar{t}$ production at the level of 52.8% for jets with $E_t > 20$ GeV and $|\eta| < 2.4$.

ATLAS results shows the importance of the full GEANT simulation and reconstruction for realistic estimation of the b-tagging performance.

7 Conclusions

We can conclude that vertex b-tagging will be the major tool for the search for low mass Higgs both in the Standard Model scheme and in its Supersymmetric extensions at LHC experiments. In particular:

- b-tagging is important for distinguishing the MSSM Higgs from SM scheme.

- Full simulation with full reconstruction tools are available now for b-tagging studies in LHC detectors.

- The rejection of gluon jets of $R_{g-jet} = 50$ with b-tagging efficiency $\epsilon_{b-jet} = 50\%$ has been achieved in the barrel part of ATLAS for full GEANT simulation and reconstruction.

- Without long-lived component in the gluon jets the rejection $r_{g-jet} = 500$ is achieved at $\epsilon_{b-jet} = 50\%$. It shows the potentiality for improvements by identifying K_s^0 and Λ decays.

More studies are needed in several fields:

- Use of the reconstructed secondary vertex in b-tagging.

- Inclusion of Z-impact parameter or use of 3-dimensional impact parameter.

- Study of the performances at high luminosity LHC runs.

- Impact of b-layer efficiency on b-tagging.

- Impact of detector noise on b-tagging.

- Dependences of b-tagging on p_T, η, jet flavour etc.

8 ACKNOWLEDGEMENTS

References

[1] ATLAS Collaboration: ATLAS Technical Proposal for a General-Purpose pp Experiment at the Large Hadron Collider at CERN, CERN/LHCC/94-43.

[2] CMS Collaboration: The Compact Muon Solenoid Technical Proposal, CERN/LHCC/94-38.

[3] A.Nisati, BEAUTY-95, *Nuclear Instruments and Methods A368 (1995) 109.*

[4] D.Kotlinski and C.Racca, BEAUTY-95, *Nuclear Instruments and Methods A368 (1995) 115.*

[5] J.L.Rosner, in B decays, ed. S.Stone, World Scientific, 1994. p.470;
A.Ali and D.London, *Z.Phys. C 65 (1995) 431.*

[6] LHC-B Letter-of-Intent, A Dedicated LHC Collider Beauty Experiment for Precision Measurements of CP-Violation, CERN/LHCC/95-5 (25 August 1995).

[7] K.T.Knopfle, VERTEX-96, These Proceedings.

[8] B.Gobbo, VERTEX-96, These Proceedings.

[9] T.Matsuda, VERTEX-96, These Proceedings.

[10] M.I.Vysotsky, V.A.Novikov, L.B.Okun and A.N.Rozanov, Electroweak radiative corrections in Z boson decays, hep-ph/9606253 (in English), *Uspekhi Fizitcheskikh Nauk 166-5, (1996) 539 (in Russian).*

[11] LEP Collaborations ALEPH, DELPHI, L3, OPAL and LEP Electroweak Working Group, A Combination of Preliminary LEP Electroweak Measurements and Constraints on the Standard Model, CERN-PPE/95-172, 24 November 1995;
LEP Experiments ALEPH, DELPHI, L3 and OPAL, Combining Heavy Flavour Electroweak Measurements at LEP, CERN-PPE/96-017, 8 February 1996.

[12] J.Ellis, C.L.Fogli and E.Lisi, The Top Quark and Higgs Boson Masses in the Standard Model and the MSSM, CERN-TH 7261/94 (1994).

[13] ALEPH Collaboration, Mass Limit for the Standard Model Higgs Boson with the full LEP-I ALEPH data sample, CERN-PPE/96-079 (1996).

[14] D.Froidevaux and E.Richter-Was, Is the channel $H \to b\bar{b}$ observable at LHC ?, CERN-TH-7459, September 1994.

[15] Comparison of the ATLAS and CMS discovery potential for the $H \to \gamma\gamma$ channel at the LHC, ATLAS Internal Note, PHYS-No-64, 28 February 1995.

[16] E.Richter-Was, D.Froidevaux, F.Gianotti et al., Minimal Supersymmetric Standard Model Higgs rates and backgrounds in ATLAS, ATLAS Internal Note, Phys-No-074, 22/04/1996.

[17] A.Rozanov, Pixel geometry description in DICE-95, ATLAS Internal Note, available at WWW at:

   `http://marpix1.in2p3.fr/pixel_dice/intro_dice.html`

[18] R.Horisberger, VERTEX-96, These Proceedings.

[19] P.Fischer et al.: Pixel detector back-up document to support the ATLAS Technical Proposal, ATLAS Internal Note, INDET-NO-086 (1994).

[20] I.Gavrilenko, ATLAS internal Notes INDET-016, INDET-055.

[21] R.Clift and A.Poppleton, IPATREC: inner detector pattern recognition and track finding, ATLAS internal Note, SOFT-No-009, 14 June 1994.

[22] A.Khanov and N.Stepanov, A Fast track Finder Algorithm:CMS Track finding Capability Estimations, CMS TN/94-309.

[23] T.Mouthuy, BEAUTY-95, *Nuclear Instruments and Methods A368 (1995) 213.*

[24] R.Brun et al., GEANT, Detector Description and Simulation Tool, CERN Program Library W5013, 1994.

[25] A.Artamonov, A.Dell'Acqua, D.Froidevaux, M.Nessi, P.Nevski and G.Poulard, DICE-95, ATLAS Internal Note, SOFT/95-14b 15 January 1996.

[26] P.Nevski, ATRECON, ATLAS Internal Note, SOFT/95-15 .

[27] I.Gavrilenko, S.Haywood, A.Clark, D.Froidevaux and L.Rossi, Present status of b-tagging studies in ATLAS, ATLAS Internal Note, INDET-No-115, 24 November 1995.

[28] S.Haywood, ATLAS Internal Note, INDET-NO-092.

Table 1: Production cross-section and rates of the $H \to b\overline{b}$ channel with $m_H = 100$ GeV and backgrounds including branching ratios for one year of low luminosity LHC run with $L = 10^4$ pb^{-1}. ϵ_b is the efficiency of b-jet tagging, while R is the rejection factor of light and gluon jets by b-tagging.

Initial state	σ_{pp}	Rate at $L = 10^4$pb^{-1}
WH	0.73 pb	$440 \times \epsilon_b^2$ events
WZ	0.86 pb	$600 \times \epsilon_b^2$ events
W b$\overline{b}$	69.3 pb	$3660 \times \epsilon_b^2$ events
$q\overline{q} \to W \to t\overline{b}$	1.42 pb	$570 \times \epsilon_b^2$ events
$t\overline{t}$	266.1 pb	$5170 \times \epsilon_b^2$ events
q g $\to$ W g $\to$ tbq	45.6 pb	$210 \times \epsilon_b^2$ events
Wjj	5480.0 pb	$5.3 \cdot 10^6 \times 1/R^2$ events

Table 2: The combination all Higgs channels in the range of $80 < m_H < 120$ GeV for three years running at low luminosity with $L = 3 \times 10^4$ pb^{-1} from the ATLAS Technical Proposal.

Higgs mass	Process	Signal	Backgd.	$S/\sqrt{B}$
$m_H = 80$ GeV	WH, $H \to b\overline{b}$	525	20 660	3.7
	$t\overline{t}$ H, $H \to b\overline{b}$	552	12 180	5.0
	$H \to \gamma\gamma$	144	14 900	1.2
	Combined			6.3
$m_H = 100$ GeV	WH, $H \to b\overline{b}$	330	17 040	2.5
	$t\overline{t}$ H, $H \to b\overline{b}$	261	10 530	2.5
	$H \to \gamma\gamma$	252	14 200	2.1
	Combined			4.2
$m_H = 120$ GeV	WH, $H \to b\overline{b}$	141	10 920	1.3
	$t\overline{t}$ H, $H \to b\overline{b}$	126	8490	1.4
	$H \to \gamma\gamma$	312	9200	3.3
	Combined			3.8

Table 3: Number of expected events and significances for low mass Higgs production for an integrated luminosity of 10^5 pb^{-1}.

Process	Signal	Backgd.	$S/\sqrt{B}$
$m_H = 80$ GeV			
$t\bar{t}$ H, H $\to$ b$\bar{b}$	1840	40 600	9.1
H $\to \gamma\gamma$	480	49 600	2.2
WH,$t\bar{t}$ H, H $\to \gamma\gamma$	15	15	3.9
Combined			10.2
$m_H = 100$ GeV			
$t\bar{t}$ H, H $\to$ b$\bar{b}$	870	35 100	4.6
H $\to \gamma\gamma$	840	47 400	3.9
WH,$t\bar{t}$ H, H $\to \gamma\gamma$	15	15	3.9
Combined			7.2
$m_H = 120$ GeV			
$t\bar{t}$ H, H $\to$ b$\bar{b}$	420	28 300	2.5
H $\to \gamma\gamma$	1040	30 700	5.9
WH,$t\bar{t}$ H, H $\to \gamma\gamma$	15	15	3.9
Combined			7.5

Table 4: Parametrised impact-parameter resolution of the ATLAS inner detector for the barrel part of the various vertexing layouts. The resolutions are given as functions of p_T in GeV and of the polar angle θ.

Vertex detector	σ_{ip} (μm)	σ_z (μm)
High luminosity	$27 \oplus \frac{220}{p_T\sqrt{\sin\theta}}$	$130 \oplus \frac{240}{p_T\sqrt{\sin\theta^3}}$
Binary pixels	$18 \oplus \frac{61}{p_T\sqrt{\sin\theta}}$	$84 \oplus \frac{130}{p_T\sqrt{\sin\theta^3}}$
Analog pixels	$12 \oplus \frac{52}{p_T\sqrt{\sin\theta}}$	$52 \oplus \frac{79}{p_T\sqrt{\sin\theta^3}}$
Micro-strips	$13 \oplus \frac{62}{p_T\sqrt{\sin\theta}}$	$39 \oplus \frac{90}{p_T\sqrt{\sin\theta^3}}$

Table 5: Track finding efficiencies using PTRA pattern recognition program on the sample of H $\rightarrow$ b$\overline{\text{b}}$ events in the barrel region for tracks with $p_T > 1$ GeV and $|\eta| < 1$.

Condition	Good tracks	Tracks with > 1 wrong hit	Lost tracks
only dE/dx	99.5%	0.0%	$< 0.5\%$
dE/dx and mult.scat.	94.8%	3.0%	2.2%
Full GEANT	92.3%	3.4%	4.3%

Figure Captions
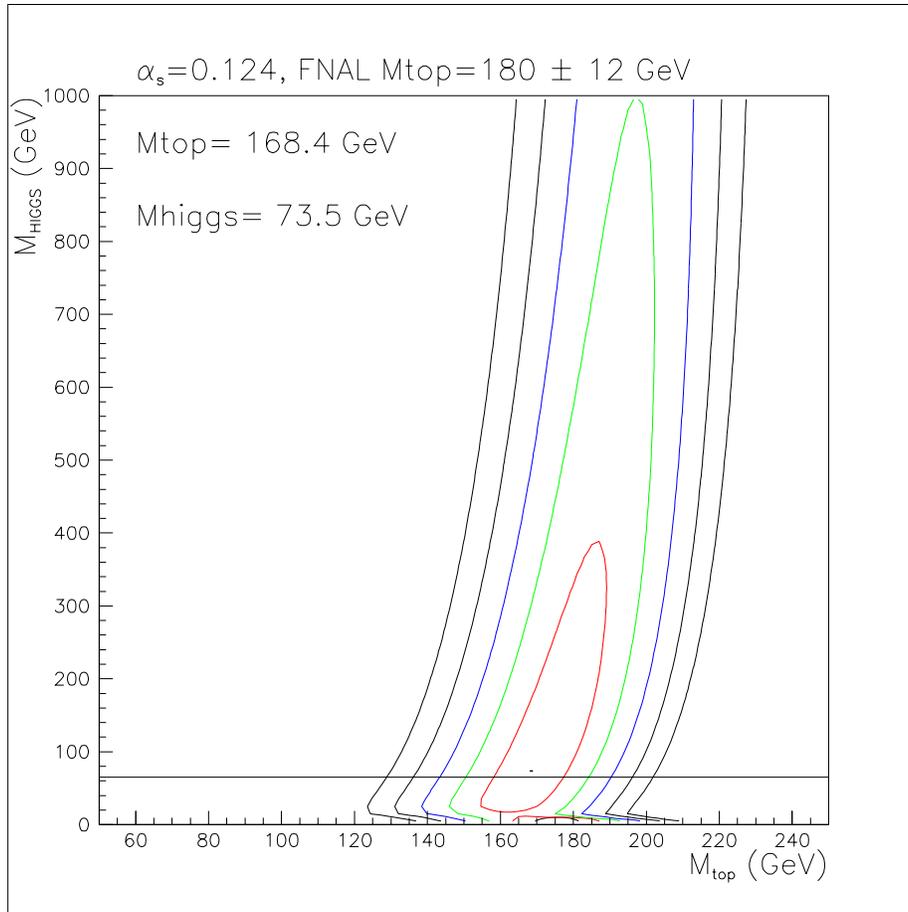
Fig.1 The allowed region of top mass and Higgs mass from the LEP-TOP fit to all precision electroweak measurements and direct measurement of t-quark mass at Fermilab. The result of the fit with $m_t = 168$ GeV and $m_H = 74$ GeV is shown as a dot. The contours corresponds to the levels of one, two, three etc. standard deviations. The limit from the direct search for Higgs at LEP is shown as a line at $m_H = 63.9$ GeV.

Fig.2 Azimuthal view on the barrel pixel vertex detector of ATLAS. Three pixel detector layers at radii of 4cm, 11cm and 14 cm are shown.

Fig.3 Longitudinal cut of the inner detector of ATLAS. Three barrel pixel layers at the radii of 4 cm, 11 cm and 14 cm and four pixel disks at z-positions of 47 cm, 64 cm, 78 cm and 107 cm are placed close to the interaction point.

Fig.4 Material budget of the ATLAS pixel detectors with and without b-layer at radius of 4 cm as a function of pseudo-rapidity η.

Fig.5 Impact parameter resolution for 100 GeV muons as a function of the pseudo-rapidity η. Analytical parametrisation for barrel ATLAS tracker from the ATLAS Technical Proposal are shown as continuous curve.

Fig.6 Impact parameter resolution for 1 GeV muons as a function of the pseudo-rapidity η. Analytical parametrisation for barrel ATLAS tracker from the ATLAS Technical Proposal are shown as continuous curve.

Fig.7 Residual distributions for ATLAS pixel test chip with CPPM readout scheme on the coordinate with 432 μm pitch. Pixel clusters with two hits are selected for the bottom histogram.

Fig.8 Residual distributions for ATLAS pixel test chip with CPPM readout scheme on the coordinate with 50 μm pitch. Pixel clusters with two hits are selected for the bottom histogram.

Fig.9 Transverse impact parameter distribution for tracks from the decay $H \rightarrow gg$ (a) and for tracks from the decay $H \rightarrow b\overline{b}$ (b) in the simulation without multiple scattering and secondary interactions. The impact parameter is signed with respect to the reconstructed jet axis.

Fig.10 Transverse impact parameter distribution for tracks from the decay $H \rightarrow gg$ (a) and for tracks from the decay $H \rightarrow b\overline{b}$ (b) in the simulation with multiple scattering and secondary interactions. The impact parameter is signed with respect to the reconstructed jet axis.

Fig.11 Gluon-jet rejection versus b-jet efficiency in ATLAS barrel inner detector with pixel b-layer obtained by track counting method with PTRA pattern recognition program. The results with partial GEANT simulation without secondary interactions are shown as open circles, the full simulation results are shown as black squares.

Figure 1: The allowed region of top mass and Higgs mass from the LEPTOP fit to all precision electroweak measurements and direct measurement of t-quark mass at Fermilab. The result of the fit with $m_t = 168$ GeV and $m_H = 74$ GeV is shown as a dot. The contours corresponds to the levels of one, two, three etc. standard deviations. The limit from the direct search for Higgs at LEP is shown as a line at $m_H = 63.9$ GeV.
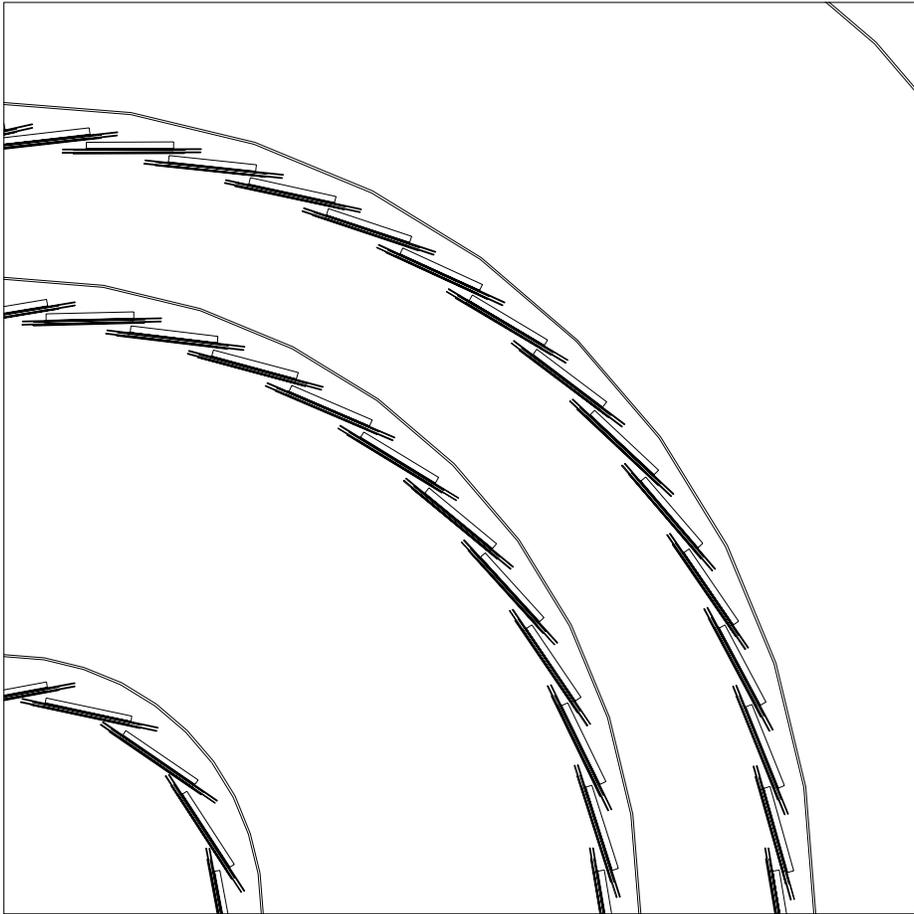
22

Figure 2: Azimuthal view on the barrel pixel vertex detector of ATLAS. Three pixel detector layers at radii of 4cm, 11cm and 14 cm are shown.

η=1.4
η=1.6
η=2.2
η=2.6
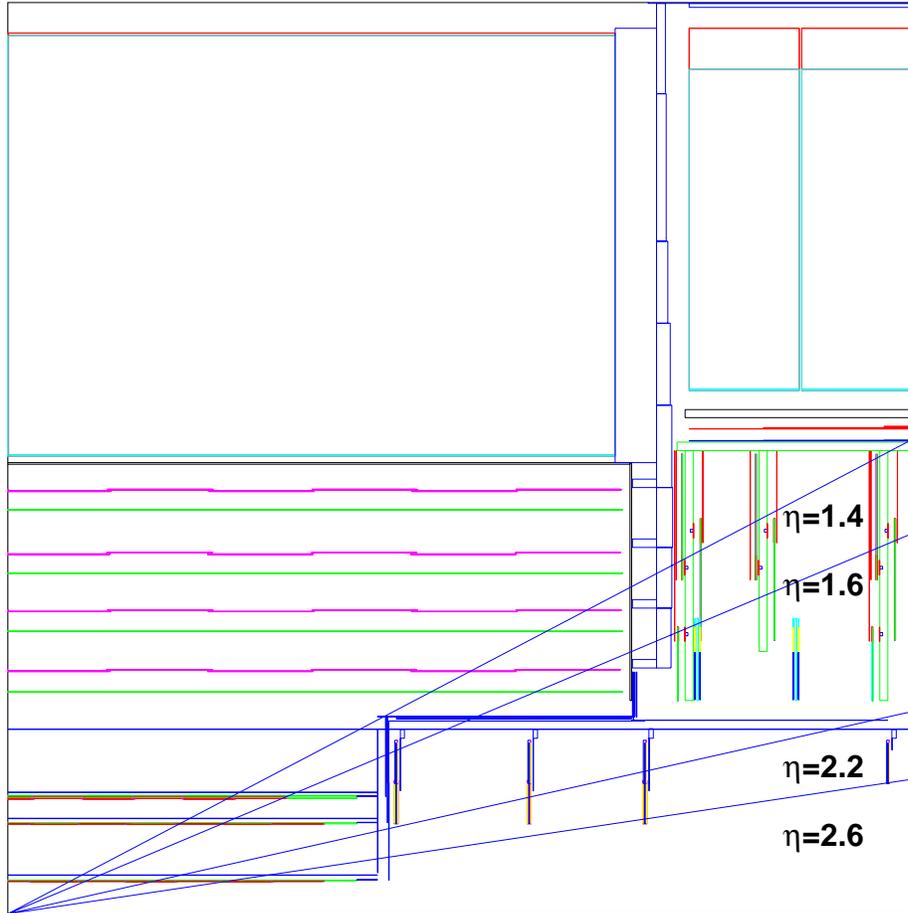
Figure 3: Longitudinal cut of the inner detector of ATLAS. Three barrel pixel layers at the radii of 4 cm, 11 cm and 14 cm and four pixel disks at z-positions of 47 cm, 64 cm, 78 cm and 107 cm are placed close to the interaction point.
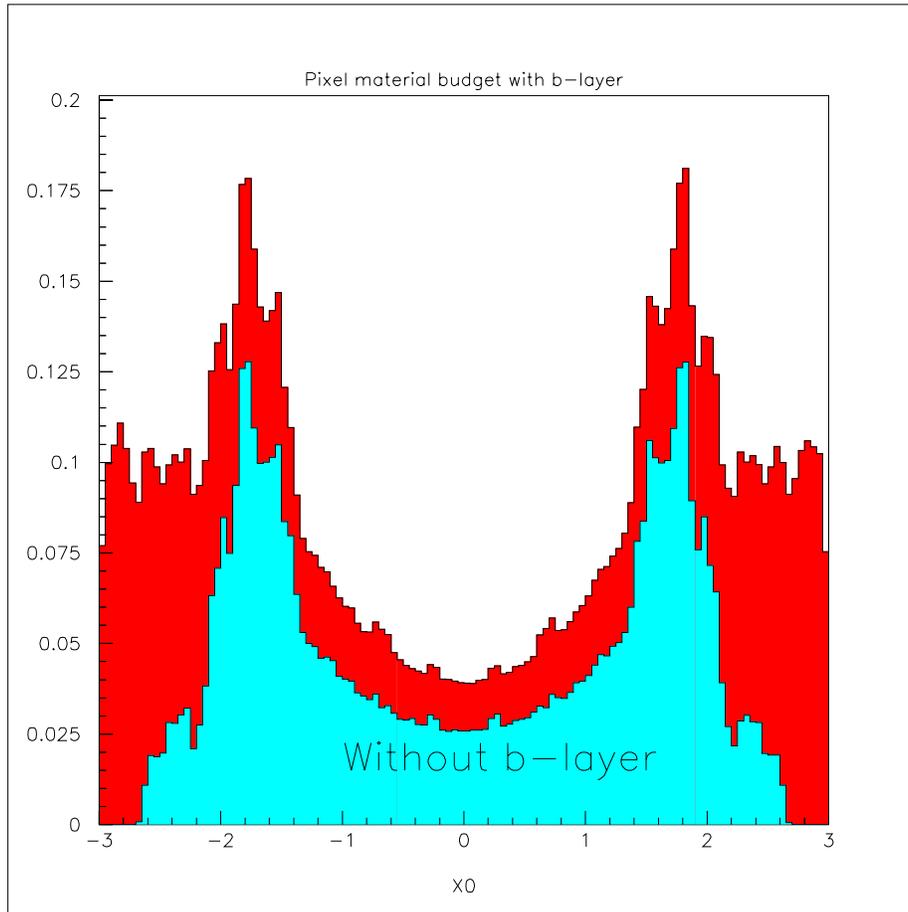
Figure 4: Material budget of the ATLAS pixel detectors with and without b-layer at radius of 4 cm as a function of pseudo-rapidity.

pixb

$$\sigma_{IP} = 18 \oplus \frac{61}{p_T \sqrt{\sin\theta}}$$

Rphi resolution vs eta

$$\sigma_Z = 84 \oplus \frac{130}{p_T \sqrt{\sin\theta^3}}$$

Z resolution vs eta
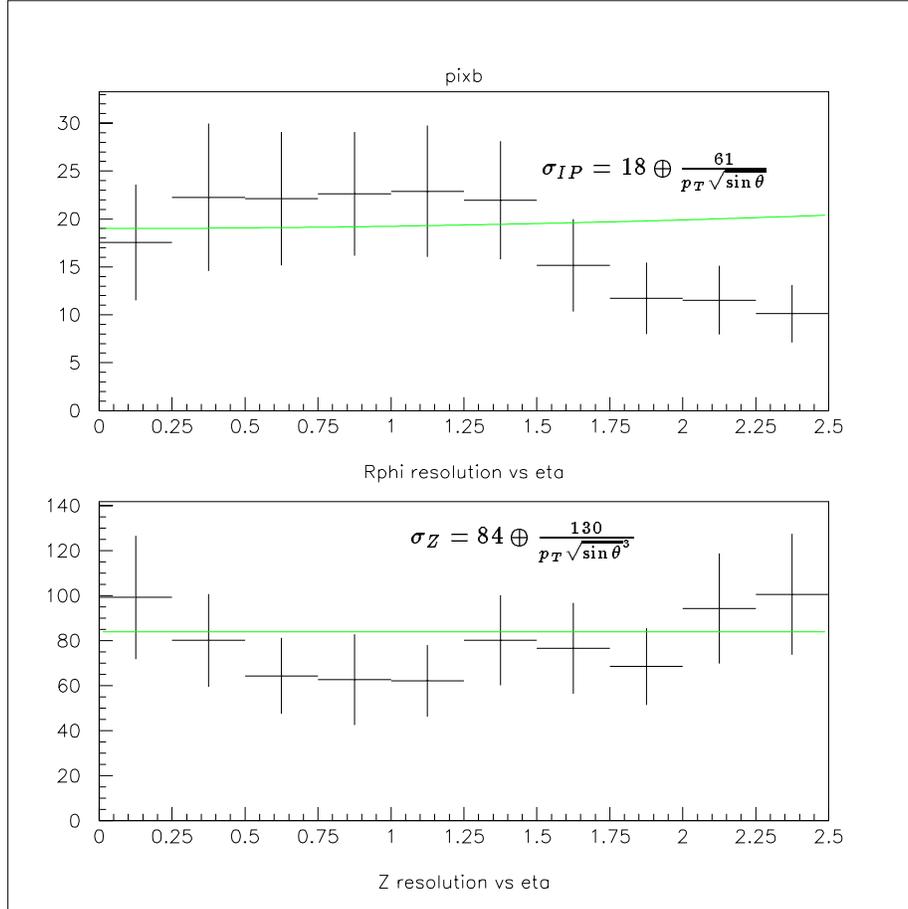
Figure 5: Impact parameter resolution for 100 GeV muons as a function of the pseudo-rapidity η. Analytical parametrisation for barrel ATLAS tracker from the ATLAS Technical Proposal are shown as continuous curve.
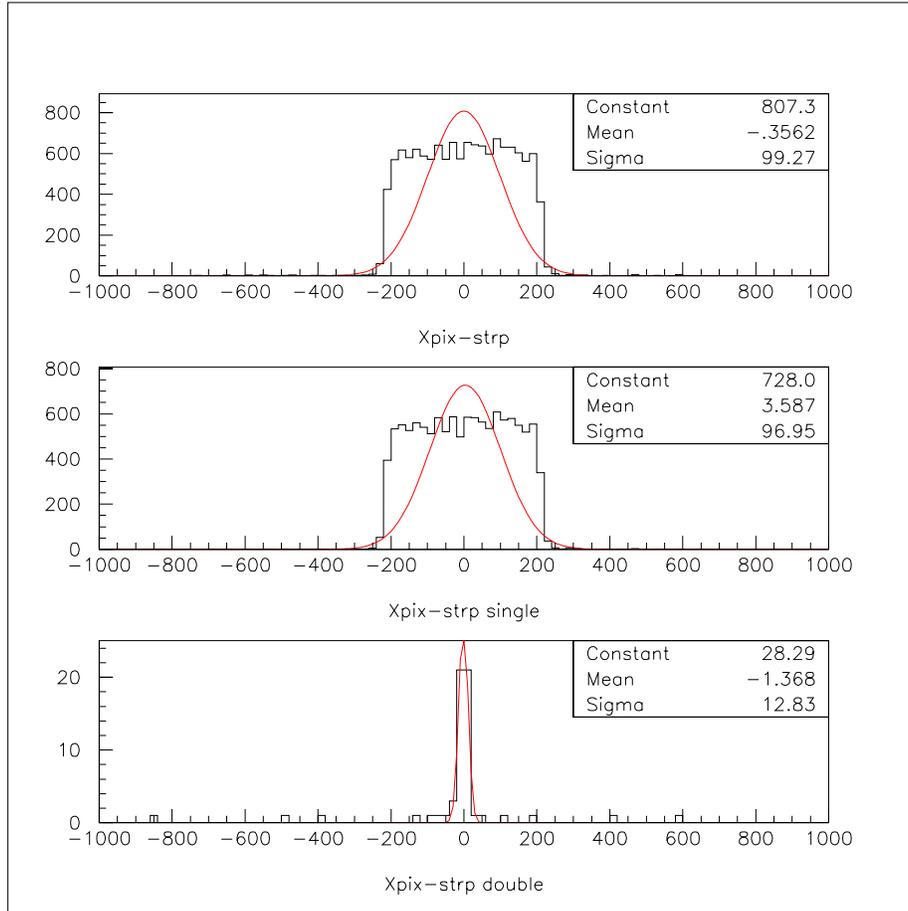
$$\sigma_{IP} = 18 \oplus \frac{61}{p_T \sqrt{\sin\theta}}$$

$$\sigma_Z = 84 \oplus \frac{130}{p_T \sqrt{\sin\theta^3}}$$
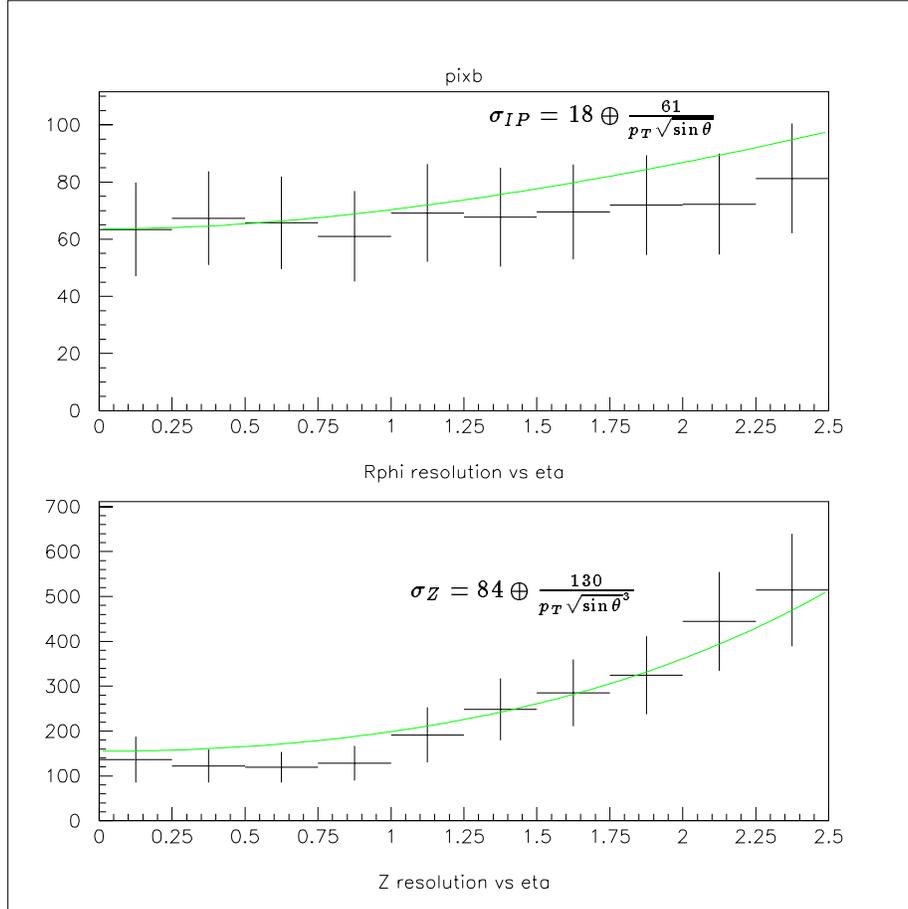
Figure 6: Impact parameter resolution for 1 GeV muons as a function of the pseudo-rapidity η. Analytical parametrisation for barrel ATLAS tracker from the ATLAS Technical Proposal are shown as continuous curve.
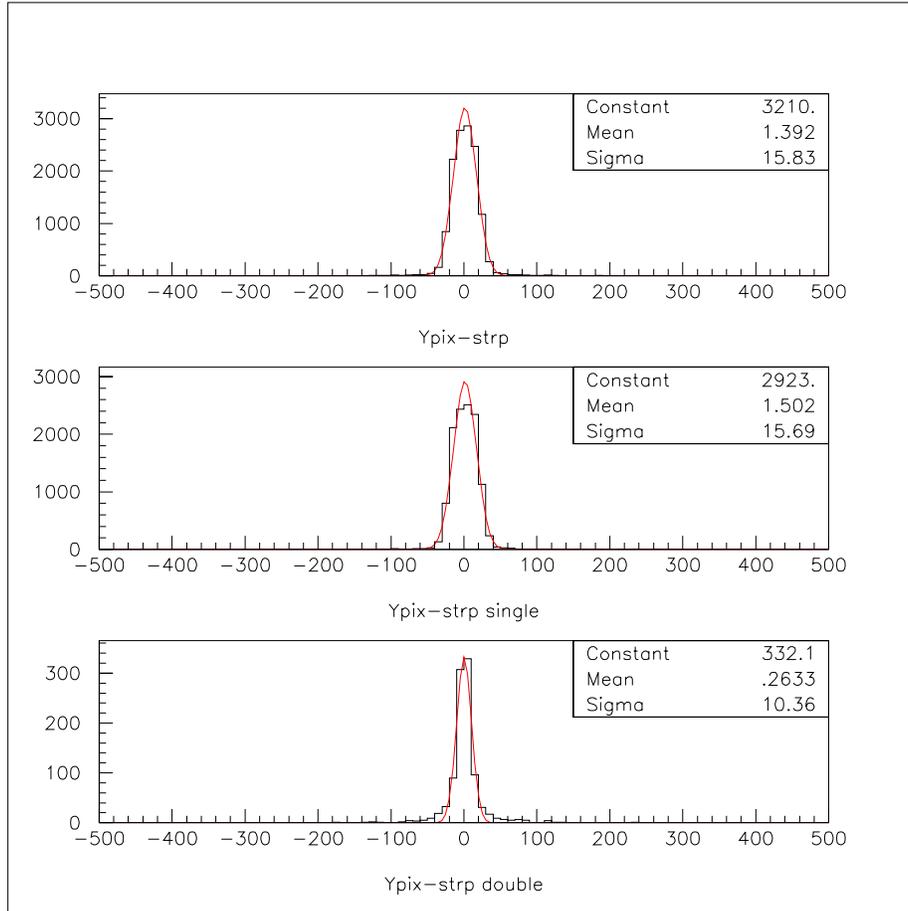
Figure 7: Residual distributions for ATLAS pixel test chip with CPPM readout scheme on the coordinate with 432 μm pitch. Pixel clusters with two hits are selected for the bottom histogram.
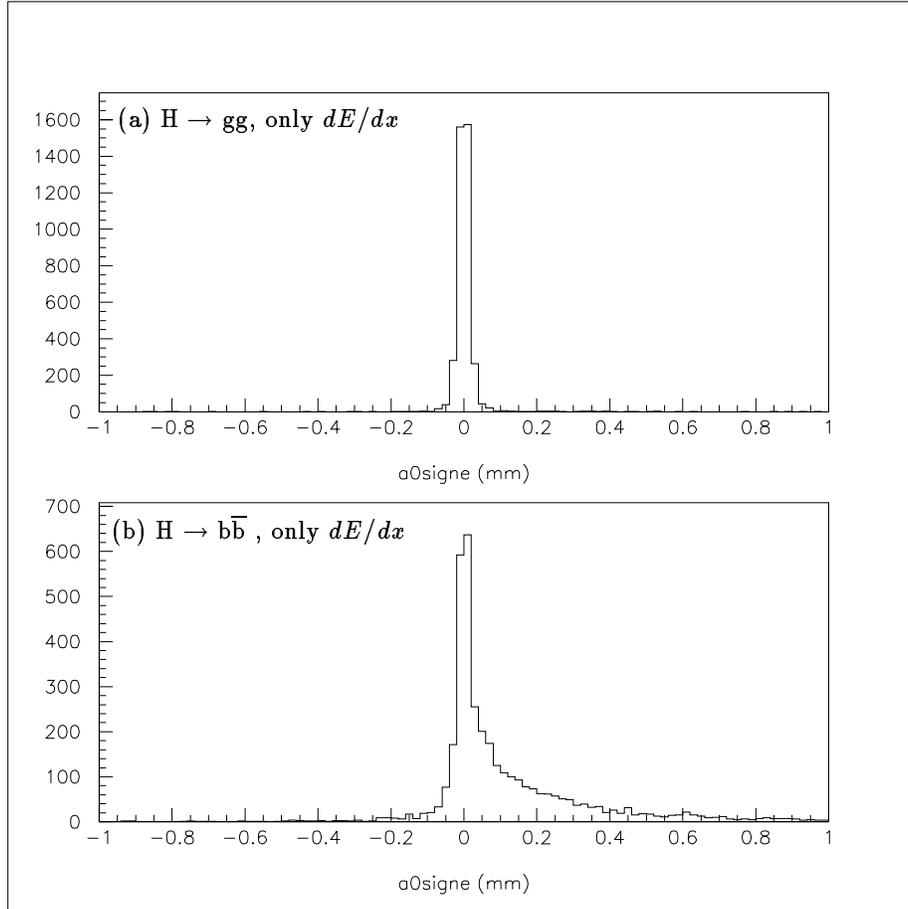
Figure 8: Residual distributions for ATLAS pixel test chip with CPPM readout scheme on the coordinate with 50 μm pitch. Pixel clusters with two hits are selected for the bottom histogram.

Figure 9: Transverse impact parameter distribution for tracks from the decay H → gg (a) and for tracks from the decay H → b$\overline{\text{b}}$ (b) in the simulation without multiple scattering and secondary interactions. The impact parameter is signed with respect to the reconstructed jet axis.
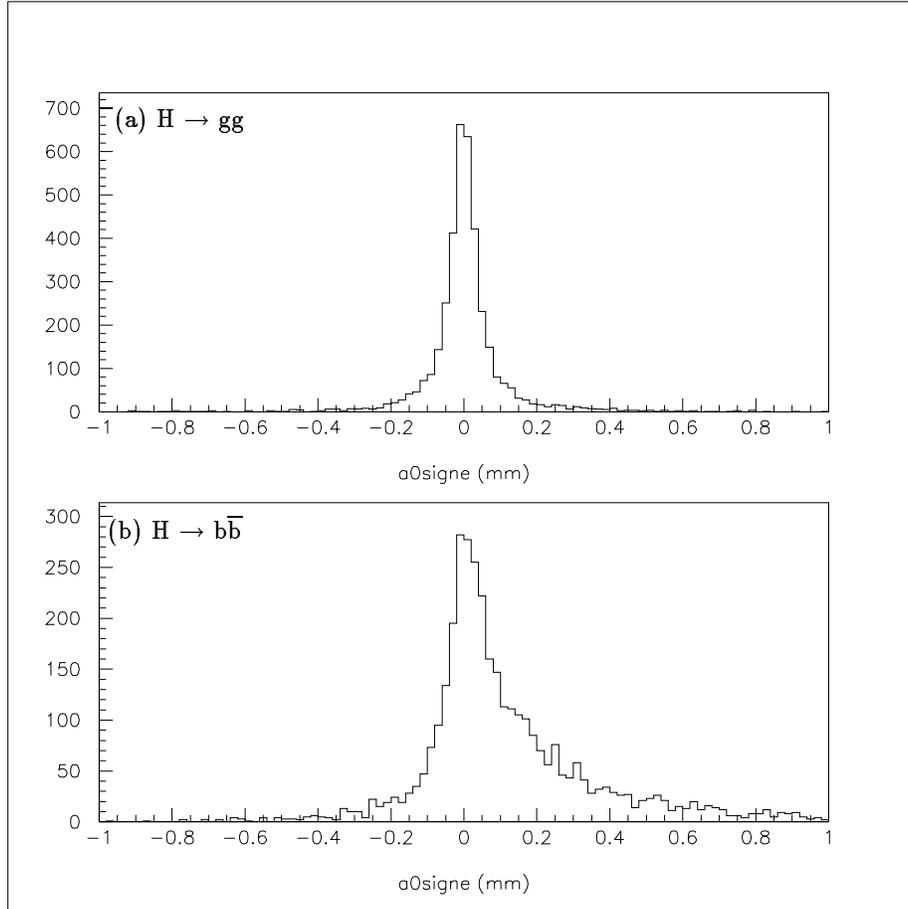
Figure 10: Transverse impact parameter distribution for tracks from the decay $H \rightarrow gg$ (a) and for tracks from the decay $H \rightarrow b\bar{b}$ (b) in the simulation with multiple scattering and secondary interactions. The impact parameter is signed with respect to the reconstructed jet axis.
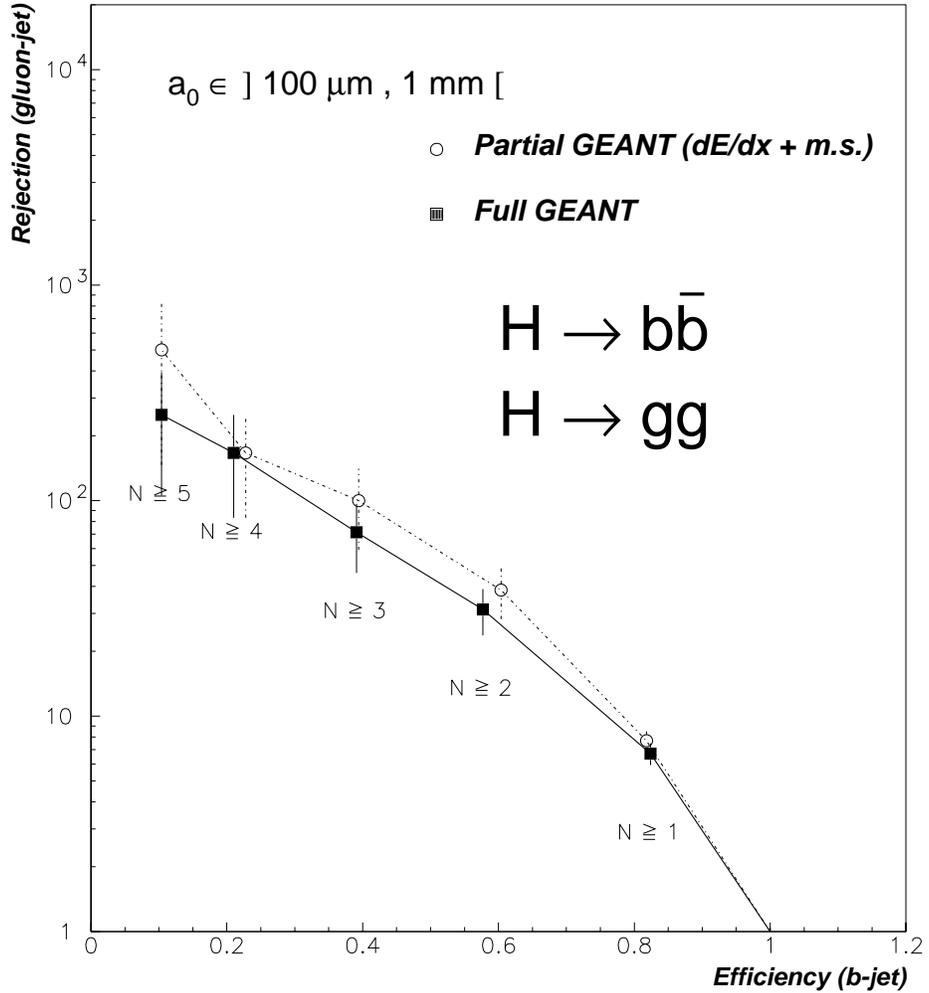
Figure 11: Gluon-jet rejection versus b-jet efficiency in ATLAS barrel inner detector with pixel b-layer obtained by track counting method with PTRA pattern recognition program. The results with partial GEANT simulation without secondary interactions are shown as open circles, the full simulation results are shown as black squares.